Aharonov-Casher Effect in Bi$_2$Se$_3$ Square-Ring Interferometers

Fanming Qu, Fan Yang, Jun Chen, Jie Shen, Yue Ding, Jiangbo Lu, Yuanjun Song, Huaixin Yang, Guangtong Liu,
Jie Fan, Yongqing Li, Zhongqing Ji, Changli Yang, and Li Lu*

*Daniel Chee Tsui Laboratory, Beijing National Laboratory for Condensed Matter Physics, Institute of Physics,
Chinese Academy of Sciences, Beijing 100190, People's Republic of China*
(Received 30 March 2011; revised manuscript received 5 May 2011; published 30 June 2011)

Electrical control of spin dynamics in Bi$_2$Se$_3$ was investigated in ring-type interferometers. Aharonov-Bohm and Altshuler-Aronov-Spivak resistance oscillations against a magnetic field, and Aharonov-Casher resistance oscillations against the gate voltage were observed in the presence of a Berry phase of π. A very large tunability of spin precession angle by the gate voltage has been obtained, indicating that Bi$_2$Se$_3$-related materials with strong spin-orbit coupling are promising candidates for constructing novel spintronic devices.

One important task of spintronics research is to explore electrical control of spin dynamics in solid-state devices via spin-orbit coupling (SOC) [1]. By tuning the applied gate voltage one can rotate the spin of a moving electron with purely electrical means rather than traditionally with magnetic fields. The devices that have been proposed and studied include the Datta-Das spin field effect transistors based on Rashba SOC [2,3], the spin interferometers and filters [4–9] via the Aharonov-Casher (AC) effect [10], and the quantum-dot spin qubits using electrical pulse to control the spin precession [11–13], etc. Since the tunability of spin rotation by applied gate voltage relies on the strength of SOC, materials with stronger SOC would preferably be chosen to construct devices in this regard.

Topological insulators (TIs) [14–16] are a new class of materials with strong SOC. The SOC in TIs is so strong that it leads to the formation of helical electron states at the surface or edge with interlocked momentum and spin degrees of freedom. Many novel properties of TIs have been observed, including the formation of Dirac fermions [17–20], suppression of backscattering [21], and the appearance of weak antilocalization (WAL) [22–26].

With such a novel electron system caused by strong SOC, electrical control of spin dynamics in TIs becomes a particularly interesting issue. Previously, Molenkamp group has studied the spin interference in a ring device made of HgTe/HgCdTe quantum well, a material which could be tuned into a two-dimensional (2D) TI, and reached a tunability higher than that in devices based on InAlAs/InGaAs two-dimensional electron gas (2DEG) [6,9]. Here we report our investigation on the electrical control of spin dynamics in a square-ring type of interferometer based on Bi$_2$Se$_3$, a material which could eventually be tuned into a 3D TI. The tunability of spin precession by gate voltage is found to be significantly higher than that reported before.

Bi$_2$Se$_3$ nanoplates were synthesized in a 2-inch horizontal tube furnace via a chemical vapor deposition method

similar to literature [27]. Figure 1(a) and 1(b) are the scanning electron microscopy image and the high-resolution transmission electron microscopy image of the single-crystalline Bi$_2$Se$_3$ nanoplates, respectively. Figure 1(c) indicates that the nanoplates were grown along [11$\bar{2}$0] direction. Figure 1(e) is the x-ray powder diffraction pattern of the nanoplates, confirming they are of Bi$_2$Se$_3$ phase. The nanoplates of several tens nm thick were transferred to highly doped Si substrates with 300 nm SiO$_2$. E-beam lithography and reactive ion etching with Ar gas at low
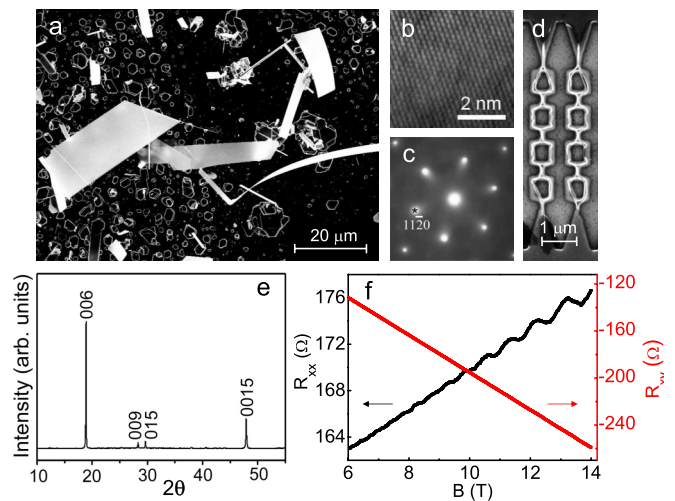
FIG. 1 (color online). (a) Scanning electron microscopy (SEM) image of the as-grown single-crystalline Bi$_2$Se$_3$ nanoplates and nanoribbons on Si substrate. (b) High-resolution transmission electron microscopy image of a nanoplate. (c) Electron diffraction pattern of a nanoplate with growth direction along [11$\bar{2}$0]. (d) SEM image of the square-ring devices. The whitish colloid on top of the rings is the residual PMMA mask. (e) X-ray powder diffraction pattern consistent with PDF cards No. 33–214 confirms the Bi$_2$Se$_3$ phase. (f) R_{xx} and R_{xy} curves of a Hall-bar fabricated on the same nanoplate connecting to device #1. The data were taken at 0.3 K.

power (20 W) were used to pattern the devices. The real interferometer devices used in this experiment contained two parallel rows of square rings, with four rings in each row, as shown in Fig. 1(d) (note that the whitish colloid is residual PMMA mask). Electron transport measurements were carried out in a sorption-pumped ^{3}He cryostat with standard lock-in technique, after Pd electrodes were fabricated to the two ends of the rows.

The data presented here were obtained from two devices with the same structure but slightly different thickness, 17 and 11 nm, labeled as device #1 and #2, respectively. For device #1, we were able to pattern a Hall bar on the same nanoplate for material characterization. Figure 1(f) shows the magnetic field dependencies of the longitudinal resistance R_{xx} and Hall resistance R_{xy} of the nanoplate at 0.3 K. Deduced from the Hall slope, $R_H = -1/ne$, the areal electron density of the nanoplate is $n = 3.9 \times 10^{13}$ cm^{-2}, corresponding to a volume density $n_{3D} = 2.3 \times 10^{19}$ cm^{-3}. Simply assuming a Drude form of sheet conductivity [28], $\sigma = ne\mu$, the effective electron mobility is estimated to be $\mu = 1000$ cm^2/V s.

Figure 2(a) shows the magnetoresistance (MR) of device #1 measured at 0.3 K. A sharp dip appears around zero magnetic field, caused by WAL of the electrons due to the existence of a Berry phase of π in the material [22–26]. The MR away from $B = 0$ demonstrates typical features of the universal conductance fluctuations (UCF), with a rough period of ~ 0.1 to 0.2 T, and a decaying amplitude with increasing both the magnetic field B and temperature T [see the inset of Fig. 2(a)]. On the UCF background, smaller but reproducible resistance oscillations at a period of ~ 0.013 T can be recognized up to the highest field of this experiment, 8 T. Figures 2(b) and 2(c) show the details of oscillations in the two marked windows in Fig. 2(a) at low and high magnetic fields, respectively.

The MR oscillations become much clearer after the UCF background is subtracted, as shown in Figs. 2(d) and 2(e). To do so, we let each data point subtract its moving averaged surroundings over ~ 0.1 T span. It can be seen that the oscillations of ΔR sustain up to the highest field of this experiment, although the amplitude decreases significantly. Fast Fourier transformation (FFT) analysis of the data from 0.2 to 8 T reveals a broad peak centered at ~ 76 T^{-1} [Fig. 2(f)]. It is in perfect agreement with the expected frequency of Aharonov-Bohm (AB) oscillations $(\Delta B)^{-1} = S/\phi_0 = 75$ T^{-1}, where $\phi_0 = h/e$ is the flux quanta, h the Planck's constant, e the electron charge, and $S = 560$ nm $\times$ 560 nm is the averaged area of the rings. The lower and upper bounds of the FFT peak, as marked by the red arrows in the figure, also correspond nicely to the areas of the outer-most and inner-most trajectories of electrons in the rings whose width is ~ 120 nm.

Figures 3(a) and 3(b) are 2D plots of ΔR as a function of magnetic field B and gate voltage V_g for devices #1 and #2, respectively. In these plots, the UCF and the predominant
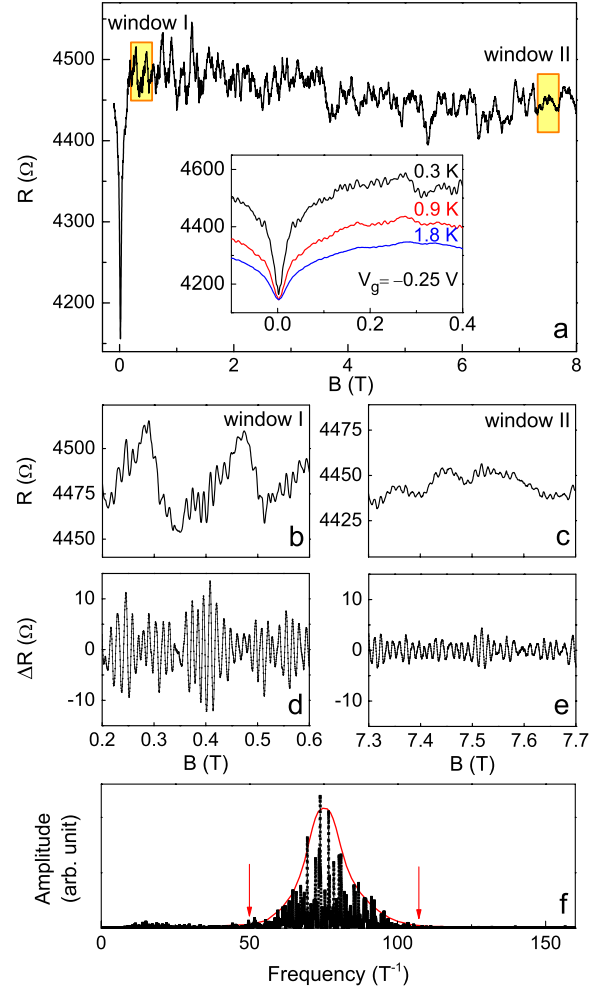
FIG. 2 (color online). (a) Magnetoresistance (MR) of device #1 measured at 0.3 K and $V_g = 0$. Inset: MR around zero field and at several different temperatures. (b) and (c): Details of MR fluctuations in low and high magnetic fields, at the two windows marked in (a), respectively. (d) and (e): MR in (b) and (c) after the UCF background is subtracted, labeled as ΔR. (f) Fast Fourier transformation (FFT) of ΔR in a field range of 0.2 to 8 T. The red line and arrows are guidance for the eyes, showing the peak position and the upper and lower bounds expected from the innermost, middle, and outermost electron trajectories of the square rings.

WAL dip at each row of the data are largely subtracted by the above mentioned treatment. Robust AB periods extending to higher fields can be clearly seen, as illustrated by the long arrows. Besides, a second type of periods with doubled frequency can also be recognized at fields below ~ 0.01 T, as indicated by the short arrows. These are the Altshuler-Aronov-Spivak (AAS) oscillations arisen from the interference of electron's wave packet circulating along the two time-reversal loops on the rings. AAS oscillation is a low field phenomenon, because the magnetic field breaks the time-reversal symmetry of the two trajectories. However, the fast decay of AAS oscillations here is largely caused by the finite width of the rings. As shown in
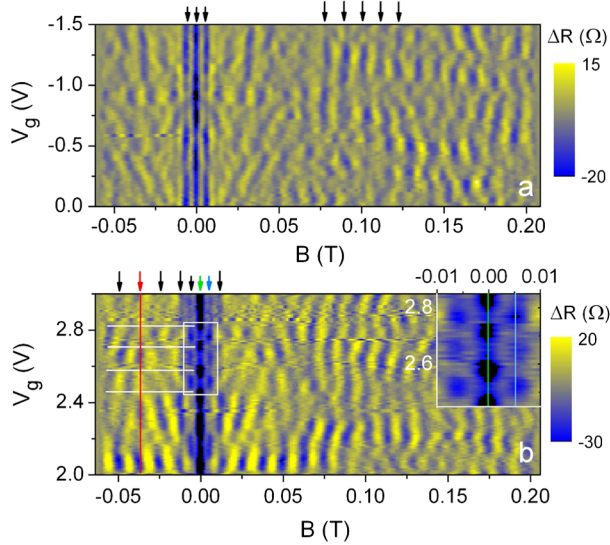
FIG. 3 (color online).   2D plots of ΔR as a function of magnetic field B and back-gate voltage V_g measured at 0.3 K for devices #1 (a) and #2 (b). The long and short arrows in both plots illustrate the B-dependent AB and AAS oscillation periods, respectively. The white lines in (b) indicate the π phase shift of the V_g-dependent AC oscillations in the AB region. The V_g-dependent oscillation frequency doubles in the AAS region. The rectangle area in (b) is magnified and shown at the upper right corner.

FIG. 4 (color online).   (a) Illustration of AB interference (red trajectories) and AAS interference (solid and dottd green loops) for charges in a square ring. The existence of SOC creates an effective magnetic field B_{so} pointing towards/ or from the center of the ring for counterclockwise (CCW)/clockwise (CW) propagation modes, which influences spin precession and generates an AC phase in addition to the AB and AAS phases. (b) $A_1(\theta)$ and $A_2(\theta)$ as a function of θ (see text). The former varies roughly at twice frequency of the latter. (c) ΔR-V_g curves taken from Fig. 3(b) at fixed fields marked by the lines and arrows of corresponding colors. The spin precession angle is modulated by 4π by varying V_g from the interval 2.16 to 2.77 V marked by the two stars. The dashed lines help illustrating the opposite phases between the green and blue curves in the AAS region.

Fig. 2(f), the expected frequencies of oscillations differ by a factor of ~ 2 between the innermost and outmost trajectories on the rings. It smears out the oscillations at high fields.

Besides the AB and AAS oscillations, one important feature demonstrated in Fig. 3 is the resistance fluctuations with varying V_g. Relatively regular oscillations can be recognized in Fig. 3(b) at fields below 0.05 T. The places where π phase shift happens are marked by the white lines in the AB oscillation region. In the AAS oscillation region where the period in B halves, the period in V_g also halves.

V_g-dependent resistance oscillations have previously been studied in circle rings [4,6,9,29,30] and square rings [5,7,8] based on 2DEG with SOC. The oscillations were attributed to V_g-modulated spin interference via SOC, and were referred to as an AC effect.

It is known that a charged particle circulating around a magnetic flux acquires an AB or AAS phase. As an electromagnetic dual, a magnetic moment circulating around an electric flux will similarly acquire an AC phase. It has been pointed out [31,32] that AB and AC phases can be understood in a unified picture by regarding Rashba and Dresselhaus SOC in two dimensions as a Yang-Mills non-Abelian gauge field, whose noncommutativity generates a phase difference (AC phase) between the two paths in a square ring.

For a more detailed analysis of the data, let us consider a 1D square ring illustrated in Fig. 4(a). The SOC induces an

effective magnetic field B_{so} perpendicular to the momentum and the electric field. For an electron of given spin orientation injected from terminal 1 and propagating along the AB or AAS trajectories, the energy dispersion relations for the cases of spin antiparallel/parallel to B_{so} are $E = \hbar^2 k^2 / 2m^* \pm \alpha k$, where m^* is the effective mass of electron and α is the Rashba SOC parameter. The spin precession angle [2] over a distance L along a straight channel is $\theta = \Delta k L = 2\alpha m^* L / \hbar^2$, here L is the side length of the square. When two partial waves propagate around the ring, the spin precession axis (B_{so}) will change directions from side to side, and the orders are different for clockwise (CW) and counterclockwise (CCW) modes, which results in an additional phase (AC phase) besides the AB/AAS phase when the two partial waves interfere at terminal 2/1, as schematically shown in Fig. 4(a). The probability of finding an electron at terminal 1 is [5]:

$$\overline{\langle \Psi_1 | \Psi_1 \rangle} = \tfrac{1}{2} + \tfrac{1}{4}(\cos^4\theta + 4\cos\theta\sin^2\theta + \cos 2\theta)\cos\phi_1$$
$$\equiv \tfrac{1}{2} + A_1(\theta)\cos\phi_1, \qquad (1)$$

where $\phi_1 = 2eBL^2/h$ is the AAS phase.

On the other hand, the probability of finding an electron at terminal 2 is [8]:

$$\overline{\langle \Psi_2 | \Psi_2 \rangle} = \frac{1}{2} + \frac{1}{4}(\sin^2\theta + \cos 2\theta)\cos\phi_2$$
$$\equiv \frac{1}{2} + A_2(\theta)\cos\phi_2 \qquad (2)$$

where $\phi_2 = eBL^2/h$ is the AB phase.

From the two equations above, the amplitudes of AAS and AB oscillations will be modulated by $A_1(\theta)$ and $A_2(\theta)$, respectively. The θ (thus V_g) dependencies of $A_1(\theta)$ and $A_2(\theta)$ are plotted in Fig. 4(b). One can see that $A_1(\theta)$, which is associated with the AAS trajectories, fluctuates roughly at twice the frequency of $A_2(\theta)$ which is associated with the AB trajectories. This is in agreement with our data. As can be seen in Fig. 4(c), among the three ΔR-V_g curves picked up in Fig. 3(b) at three fixed fields (marked by lines and arrows of corresponding colors), the green and blue ones picked up from the AAS region oscillate roughly at a doubled frequency compared to the red one which is picked up from the AB region.

The tunability of V_g can be estimated as follows. By comparing the data in Fig. 4(c) to the curves in Fig. 4(b), the spin precession angle is modulated by 4π between a V_g span of 2.16 to 2.77 V (marked by the two stars), so that $\Delta\theta/\Delta V_g = 6.6\pi/\text{V}$. Since $\theta = 2\alpha m^* L/\hbar^2$, the tunability of V_g on α is $\Delta\alpha/\Delta V_g = (\hbar^2/2m^*)\Delta\theta/L\Delta V_g = 11$ (peV m)/V (where $m^* = 0.13 m_e$ for Bi$_2$Se$_3$ [33]). Thus, the tunability of our Bi$_2$Se$_3$ devices is an order of magnitude larger than that of InAlAs/InGaAs devices [6,7], and is estimated to be more than 2 times larger than that of HgTe/HgCdTe devices [9]. If taking the thickness of the insulating layer into account (e.g., 300 nm for our Bi$_2$Se$_3$ devices, 50 to 100 nm for InAlAs/InGaAs devices, and 100 to 200 nm for HgTe/HgCdTe devices), the tunability here is even higher.

It has to be noted that this work does not establish that the findings here are unique to a topological insulator. With an areal carrier concentration of 3.9×10^{13} cm^{-2}, the surface electron states will coexist with the bulk states and the band-bending induced 2DEG states [34] in Bi$_2$Se$_3$. The Fermi wavelength in the bulk is estimated to be comparable to the thickness of the nanoplates, so that all types of states will be influenced by V_g, not only on their concentration but also on spin precession. If there are frequent scattering events between these states, the tunability measured should represent an averaged value over all the states. Otherwise, the type of states with higher tunability was detected.

To summarize, Bi$_2$Se$_3$ is a very promising material in terms of electrical control of spin dynamics. The appearance of AB, AAS, and AC quantum interferences in Bi$_2$Se$_3$ ring structures would allow more sophisticated multiple-degree controls of spins in specially designed devices, to realize novel functionalities such as possible non-Abelian operations on spins.

*Corresponding author.
lilu@iphy.ac.cn

[1] I. Žutić, J. Fabian, and S. D. Sarma, Rev. Mod. Phys. **76**, 323 (2004).
[2] S. Datta and B. Das, Appl. Phys. Lett. **56**, 665 (1990).
[3] H. C. Koo et al., Science **325**, 1515 (2009).
[4] J. Nitta, F. Meijer, and H. Yakayanagi, Appl. Phys. Lett. **75**, 695 (1999).
[5] T. Koga, J. Nitta, and M. van Veenhuizen, Phys. Rev. B **70**, 161302(R) (2004).
[6] T. Bergsten et al., Phys. Rev. Lett. **97**, 196803 (2006).
[7] T. Koga, Y. Sekine, and J. Nitta, Phys. Rev. B **74**, 041302(R) (2006).
[8] Z. Y. Zhu et al., Phys. Rev. B **74**, 085327 (2006).
[9] M. König et al., Phys. Rev. Lett. **96**, 076804 (2006).
[10] Y. Aharonov and A. Casher, Phys. Rev. Lett. **53**, 319 (1984).
[11] K. Ono et al., Science **297**, 1313 (2002).
[12] J. R. Petta et al., Science **309**, 2180 (2005).
[13] K. C. Nowack et al., Science **318**, 1430 (2007).
[14] X. L. Qi and S. C. Zhang, Phys. Today **63**, 33 (2010).
[15] M. Z. Hasan and C. L. Kane, Rev. Mod. Phys. **82**, 3045 (2010) and references therein.
[16] J. E. Moore, Nature (London) **464**, 194 (2010) and references therein.
[17] Y. Xia et al., Nature Phys. **5**, 398 (2009).
[18] Y. L. Chen et al., Science **325**, 178 (2009).
[19] Y. Zhang et al., Nature Phys. **6**, 584 (2010).
[20] D. Hsieh et al., Nature (London) **460**, 1101 (2009).
[21] T. Zhang et al., Phys. Rev. Lett. **103**, 266803 (2009).
[22] J. G. Checkelsky et al., Phys. Rev. Lett. **103**, 246601 (2009).
[23] J. Chen et al., Phys. Rev. Lett. **105**, 176602 (2010).
[24] M. H. Liu et al., Phys. Rev. B **83**, 165440 (2011).
[25] H. T. He et al., Phys. Rev. Lett. **106**, 166805 (2011).
[26] J. Wang et al., arXiv:1012.0271.
[27] H. L. Peng et al., Nature Mater. **9**, 225 (2009).
[28] N. W. Ashcroft and N. D. Mermin, *Solid State Physics* (Thomson Learning, Inc., Singapore, 1976), Chap. 1.
[29] A. A. Kovalev et al., Phys. Rev. B **76**, 125307 (2007).
[30] D. Frustaglia and K. Richter, Phys. Rev. B **69**, 235310 (2004).
[31] P. Q. Jin, Y. Q. Li, and F. C. Zhang, J. Phys. A **39**, 7115 (2006).
[32] N. Hatano, R. Shirasaki, and H. Nakamura, Phys. Rev. A **75**, 032107 (2007).
[33] J. G. Analytis et al., Phys. Rev. B **81**, 205407 (2010).
[34] M. Bianchi et al., Nature Commun. **1**, 128 (2010).